J. Fluid Mech. (2001), *vol.* 438, *pp.* 41–66. Printed in the United Kingdom

Computations of fully nonlinear three-dimensional wave–wave and wave–body interactions. Part 2. Nonlinear waves and forces on a body

By YUMING LIU, MING XUE† AND DICK K. P. YUE

Department of Ocean Engineering, Massachusetts Institute of Technology, Cambridge, MA 02139, USA

(Received 26 July 1999 and in revised form 22 December 2000)

The mixed-Eulerian–Lagrangian method using high-order boundary elements, described in Xue *et al.* (2001) for the simulation of fully nonlinear three-dimensional wave–wave and wave–body interactions, is here extended and applied to the study of two nonlinear three-dimensional wave–body problems: (*a*) the development of bow waves on an advancing ship; and (*b*) the steep wave diffraction and nonlinear high-harmonic loads on a surface-piercing vertical cylinder. For (*a*), we obtain convergent steady-state bow wave profiles for a flared wedge, and the Wigley and Series 60 hulls. We compare our predictions with experimental measurements and find good agreement. It is shown that upstream influence, typically not accounted for in quasi-two-dimensional theory, plays an important role in bow wave prediction even for fine bows. For (*b*), the primary interest is in the higher-harmonic 'ringing' excitations observed and quantified in experiments. From simulations, we obtain fully nonlinear steady-state force histories on the cylinder in incident Stokes waves. Fourier analysis of such histories provides accurate predictions of harmonic loads for which excellent comparisons to experiments are obtained even at third order. This confirms that 'ringing' excitations are directly a result of nonlinear wave diffraction.

1. Introduction

Nonlinear interaction of steep surface waves with large floating structures is a complex and challenging hydrodynamic problem of fundamental and practical interest in naval architecture and ocean engineering. Although linearized theory is often sufficient for routine design, it is precisely the conditions of extreme loads and motions essential to the critical performance, safety, and even survival of such structures, for which nonlinear effects are important. Despite this, fully nonlinear three-dimensional results are at present limited due to theoretical complexity and computational burden (see Tsai & Yue 1996 for a review).

In this work, we apply the mixed-Eulerian–Lagrangian (MEL) high-order boundary element method for fully nonlinear three-dimensional wave–wave and wave–body interactions (described in Xue *et al.* 2001, hereafter Part 1) to investigate two nonlinear wave–body problems of practical importance: (*a*) the generation of three-dimensional ship bow waves; and (*b*) high-frequency 'ringing' loads on a surface-piercing vertical cylinder in incident Stokes waves.

† Currently with Salomon Smith Barney, New York, USA.

Steep bow waves are ubiquitous and prominent features of an advancing ship. The modelling of such steep three-dimensional waves and their interactions with ship bows is of importance to the prediction of wave resistance, deck wetness, and ship motions. Existing studies of this problem are generally two-dimensional or quasi-two-dimensional (e.g. Grosenbaugh & Yeung 1989; Maruo & Song 1994; Tulin & Wu 1996) typically based on strip-theory or slender-body approximations. The importance of wave–body nonlinearity and three-dimensionality (e.g. upstream influence) for this problem, however, cannot generally be ignored (see e.g. Raven 1993; Fontaine & Faltinsen 1997). In this paper, we conduct time-domain fully nonlinear simulations of three-dimensional bow waves of different ship hull geometries. To isolate the effect of three-dimensionality, we first consider a canonical flared wedge bow and compare three-dimensional MEL results to quasi-two-dimensional predictions based on the slender-body approximation. For more realistic geometries, we study the Wigley and Series 60 hulls and compare steady-state results of the nonlinear simulations to available experimental bow-wave measurements, and contrast these to approximate (two-dimensional and quasi-two-dimensional) calculations. Our simulations show that upstream influence, not generally accounted for in the approximate theories, plays a critical role in three-dimensional bow-wave formation even for relatively fine bows.

Large *compliant* offshore structures with high-natural-frequency low-damping resonances are often observed to be excited by high-harmonic nonlinear wave loads. Such phenomena are termed 'ringing' and have been reported in a number of recent studies (e.g. Davies, Leverette & Spillane 1994; Krokstad & Stansberg 1995; Chaplin, Rainey & Yemm 1997). (Note that although 'ringing' phenomena are often observed in irregular seas, in this paper we use the term 'ringing' to denote the response to a high-frequency component of a regular wave field.) To evaluate the importance of nonlinear diffraction effects to ringing excitation, frequency-domain (regular) perturbation analysis can be extended to higher order. The extension to second order is now well established (e.g. Kim & Yue 1989; Chau & Eatock Taylor 1992). The observation that ringing often occurs at the third (or even higher) harmonic of the fundamental incident frequency stimulated recent perturbation analysis at the third order. These include the third-order diffraction theory of Faltinsen, Newman & Vinje (1995), who made a further assumption of long incident waves; and Malenica & Molin (1995), who solved the problem for arbitrary incident wavelength. Both theories apply (only) to the case of a vertical circular cylinder in a regular (mono-chromatic) incident wave. Faltinsen *et al.* (1995) and Malenica & Molin (1995) differ appreciably in the magnitude of the third-order force except for very small incident frequency, but markedly in the phase of that force. In addition to expected difficulties in extending such theories to more general geometries, fully nonlinear effects for steep waves may also limit the usefulness of such perturbation approaches (cf. figure 17). Given the analytic complexity even at third order, extension to higher orders (which may be called for) is formidable. Recently, Rainey (1995) refined Morison's formula to include third-order effects of the incident wave field. Chaplin *et al.* (1997) showed that this simple model tends to substantially over-estimate the ringing wave excitation even for a small cylinder.

Given the physical nature of this problem, a perhaps more efficacious approach is to tackle the nonlinear wave–body interaction problem in the time domain directly and then obtain the harmonic forcing of interest from the nonlinear steady-state force history. In this direction, Ferrant (1996) developed a linear boundary-element method based on the semi-Lagrangian formulation and applied it to study the problem of wave diffraction of mild long waves by a bottom-mounted vertical cylinder. In this

study, we perform a fully nonlinear time-domain simulation of the diffraction of Stokes incident waves by a surface-piercing vertical cylinder. We obtain steady-state time histories of the nonlinear wave loads on the cylinder from which high-harmonic (ringing) force components are extracted using Fourier analyses. The results are compared to available experimental measurements up to the third harmonic with remarkable good agreement.

The rest of the paper is organized as follows. In § 2, the treatment of the pertinent numerical issues in three-dimensional MEL simulations of fully nonlinear wave–body interactions is described. In § 3, the study of three-dimensional ship bow waves is presented. The simulation results of ringing loads and fully nonlinear wave run-up on a vertical cylinder are presented in § 4. In § 5, conclusions are given.

2. Numerical method

The mixed-Eulerian–Lagrangian (MEL) method for fully nonlinear three-dimensional wave–wave and wave–body interactions using quadratic boundary elements is given in Part 1. The method is here extended to the study of nonlinear wave-making/diffraction by surface bodies. We do not repeat here the overall formulation of the mathematical problem or the computational methodology, but outline in this section treatment of specific computational issues associated with nonlinear wave interactions with surface-piercing bodies.

2.1. *Double-node technique for intersections*

In solving the boundary-value problem (BVP) using the quadratic-boundary-element method (QBEM), a 'double-node' technique is adopted to treat the confluence of different types of boundary conditions (at the intersection of free and body surfaces), as well as the discontinuity of surface slopes (at body edges). In the MEL approach, Dirichlet (D) and Neumann (N) boundary conditions (for the velocity potential) are specified on the free surface ($\mathscr{F}$) and body surfaces ($\mathscr{B}$) respectively. At $\mathscr{F}$–$\mathscr{B}$ intersections, which may have surface slope discontinuities, we have a confluence of boundary conditions of a D–N type. At such a confluence, the solution to the BVP generally exhibits a weak singularity (Lewy 1950) which results in a degradation of the numerical solution in the absence of special treatment. A robust treatment is to use the double-node technique (e.g. Lin, Newman & Yue 1984; Dommermuth & Yue 1987) whereby both the D and N conditions are specified at $\mathscr{F} \cap \mathscr{B}$. This requires the specification of unknowns at the edges of the boundary elements, which QBEM provides. Double nodes are also required on edges of the body surface $\mathscr{B}$ where slopes are discontinuous. Because of the N–N boundary conditions, such nodes are denoted as N–N double nodes. In some applications, such body edges intersect the free surface (the bow stem is such an example), and the $\mathscr{B}$–$\mathscr{B}$–$\mathscr{F}$ point requires specification of triple (N–N–D) nodes. For simplicity, all repeated nodes are hereafter referred to as 'double-nodes'.

In the double-node technique, the nodes coincide but belong to different surfaces possessing either different boundary conditions and/or different surface normals. Thus the node belonging to a certain surface is otherwise treated like other (interior) nodes of that surface. At a $\mathscr{F} \cap \mathscr{B}$ point, for example, three variables are in general involved: the potential ϕ, and its derivatives $\nabla\phi \cdot \boldsymbol{n}$ with respect to the normals ($\boldsymbol{n}$) to $\mathscr{F}$ and $\mathscr{B}$ respectively. A D–N double node there specifies the D and N boundary conditions for ϕ and its derivative with respect to the $\mathscr{B}$-normal at that point. Collocation at that point provides a single equation for the unknown $\mathscr{F}$-normal derivative of

	Intersections	Double-node type	Unknowns
Ship bow waves	$\mathscr{F} \cap \mathscr{B}$	D–N	$\nabla\phi \cdot \boldsymbol{n}_{\mathscr{F}}$
	$\mathscr{B} \cap \mathscr{B} \cap \mathscr{F}$	N–N–D	$\nabla\phi \cdot \boldsymbol{n}_{\mathscr{F}}$
	$\mathscr{B} \cap \mathscr{B}$	N–N	ϕ
Nonlinear wave diffraction	$\mathscr{F} \cap \mathscr{B}$	D–N	$\nabla\phi \cdot \boldsymbol{n}_{\mathscr{F}}$
	$\mathscr{B} \cap \mathscr{B}$	N–N	ϕ

TABLE 1. Summary of the double-node types and the associated unknowns at the intersections of the free-surface ($\mathscr{F}$) and body ($\mathscr{B}$) and body edges for the ship bow waves (§3) and nonlinear wave diffraction (§4) problems. (D: Dirichlet; N: Neumann; and $\boldsymbol{n}_{\mathscr{F}}$: unit normal of $\mathscr{F}$.)

the potential. Similar multiple-node treatments of the N–N, D–N–N, N–N–N, ..., types can be worked out for intersections involving $\mathscr{F}$ and (discontinuous slope) $\mathscr{B}$ surfaces. In all cases, at each node point, there remains a single unknown involving the potential or its derivative with respect to a specified normal, which can be solved for by a collocation of the integral equation (equation (2.6) of Part 1) at that point. For the two problems considered in this paper, ship-bow waves (§3) and nonlinear wave loads on a vertical surface-piercing cylinder (§4), node types and unknowns at the intersections involved are summarized in table 1. More details can be found in Xue (1997).

2.2. *Intersection updating*

Proper updating of the free-surface intersection with a floating body during the MEL simulation is of importance to the global accuracy of the simulation and critically to the prediction of wave run-up and loads on the body.

For continuous flow, points on the $\mathscr{F}$–$\mathscr{B}$ intersection line must, at all times, remain on both (*a*) the body surface; and (*b*) the free surface. In MEL, the evolution of the positions of these points is required. In a direct integration of the Lagrangian equation (equation (2.4) of Part 1) for these new positions, neither (*a*) or (*b*) is guaranteed, even for very small time steps. This leads (eventually) to a breakdown of the overall simulation. To overcome this difficulty associated with surface-piercing bodies, we develop a general scheme for updating the free-surface intersection points (applicable in three dimensions).

To satisfy condition (*a*), we impose the velocity of an intersection point P, $\boldsymbol{V}_p$, to be always along the tangential direction, $\boldsymbol{e}_\tau$, of the body surface. Here $\boldsymbol{e}_\tau$ denotes a unit tangential vector on the body surface at P. For three-dimensional problems, $\boldsymbol{e}_\tau$ is non-unique although either choice of the unit tangential vector will assure (*a*). In practice, we choose $\boldsymbol{e}_\tau$ to be that which is closest to the Lagrangian velocity at that point.

To satisfy condition (*b*), we now choose the magnitude of $\boldsymbol{V}_p$ to be given by

$$\boldsymbol{V}_p = \frac{\nabla\phi \cdot \boldsymbol{n}_{\mathscr{F}}}{\boldsymbol{e}_\tau \cdot \boldsymbol{n}_{\mathscr{F}}} \tag{2.1}$$

where $\boldsymbol{n}_{\mathscr{F}}$ is the unit normal vector to the free surface at P. Note that the classical Eulerian and Lagrangian forms of the intersection point velocities can be recovered from (2.1) if we set $\boldsymbol{e}_\tau = (0, 0, 1)$ and $\nabla\phi/|\nabla\phi|$, respectively.

The potential at the new position of the intersection point can be obtained by

direct time integration:

$$\frac{\mathrm{d}\phi}{\mathrm{d}t} = \frac{\partial\phi}{\partial t} + \boldsymbol{V}_p \cdot \nabla\phi \tag{2.2}$$

where $\mathrm{d}/\mathrm{d}t$ is the substantial time derivative. For a moving body, the velocity of the intersection point can be written in the form

$$\boldsymbol{V}_p = \frac{(\nabla\phi - \boldsymbol{U}) \cdot \boldsymbol{n}_{\mathscr{F}}}{\boldsymbol{e}_\tau \cdot \boldsymbol{n}_{\mathscr{F}}} \boldsymbol{e}_\tau + \boldsymbol{U} \tag{2.3}$$

where $\boldsymbol{U}$ is the velocity of the body at P.

2.3. *Far-field closure*

For all but very short duration simulations, a satisfactory treatment of the far-field closure is essential for wave–body interaction problems in an unbounded domain. In three dimensions, where the energy density of the scattered wave must decrease with radial distance, a far-field matching technique has been found effective and was used by Dommermuth & Yue (1987) (in vertically axisymmetric flow problems). In the present work, we develop two additional schemes using doubly periodic boundaries and a sponge layer which are much simpler to implement.

Doubly periodic boundary conditions in the horizontal directions are implemented readily using the doubly-periodic (Rankine) Green function (Part 1, § 2.4). The extent of the computational domain is generally a function of the simulation duration – the simulation should be stopped before scattered waves from fictitious 'periodic' bodies arrive. In practice, for a given simulation time, the size of the computational domain is simply increased until the results in question no longer change. Examples of such convergence results can be found in Xue (1997). In this paper, this technique is applied to the problem of nonlinear wave diffraction by a vertical surface-piercing cylinder (§ 4).

Another simple far-field closure scheme which avoids the added computational effort associated with the evaluation of the doubly periodic Green function is the use of a numerical sponge layer (see e.g. Nakos, Kring & Sclavounos 1993; Clément 1996). In the present three-dimensional implementation, we place a sponge layer in a strip around the perimeter of the (rectangular) computational domain centred at the body. Within the sponge layer, we introduce artificial linear damping terms into the kinematic and dynamic boundary conditions on the free surface $\mathscr{F}$:

$$\frac{\mathrm{D}\boldsymbol{x}}{\mathrm{D}t} = \nabla\phi - \nu(x, y)(\boldsymbol{x} - \boldsymbol{x}_I), \qquad \boldsymbol{x} \in \mathscr{F}, \tag{2.4}$$

$$\frac{\mathrm{D}\phi}{\mathrm{D}t} = \tfrac{1}{2}|\nabla\phi|^2 - z - \nu(x, y)(\phi - \phi_I), \qquad \boldsymbol{x} \in \mathscr{F}, \tag{2.5}$$

where $\mathrm{D}/\mathrm{D}t$ is the Lagrangian (material) time derivative; $\boldsymbol{x}_I$ and ϕ_I are the free-surface position and velocity potential of the incident/ambient flow; and ν is an empirical damping coefficient which is in general a function of space. In this paper, this scheme is used in the calculation of ship bow waves (§ 3). Details of the implementation and documentation of the effectiveness of this scheme can be found in Xue (1997).

2.4. *Free-surface and body grid (re)generation*

In the MEL approach, Lagrangian particles on the free surface tend to cluster in regions of high flow gradients. Such clustering may lead to stronger 'saw-tooth' instability (which can be removed by smoothing), but more importantly, causes

severe distortions of the boundary elements, which become critical for the three-dimensional problem. Thus, in the absence of robust regridding of free-surface and body boundary elements, MEL simulations involving all but the simplest geometries in three dimensions rapidly break down.

To effectively resolve this problem, we extend the regridding algorithm applied by Dommermuth & Yue (1987) for axisymmetric flows to fully three dimensions. Cubic splines in both parametric directions are employed to create new sets of optimally spaced (in arclength) grid points on the free surface and on the body. Such grid regeneration in conjunction with updating of the free-surface body intersection line is an essential feature of fully nonlinear simulations involving changing wetted body surfaces. For optimal spacing in grid regeneration, we use elliptical generators with controlling factors on the free surface and transfinite interpolations on the body.

2.5. *Initial condition for the wave diffraction problem*

In the fully nonlinear simulation of wave diffraction by a body, the prescribed incident wave field is in general not compatible with the requisite (zero-flux) body boundary condition. In the absence of an effective remedy, large transients are introduced at initial time(s) which can lead to breakdown of the nonlinear simulation. This is particularly critical for a surface-piercing body where errors tend to be concentrated at the $\mathscr{F}$–$\mathscr{B}$ intersection(s).

To resolve this difficulty, a number of treatments have been implemented and evaluated. These include: (i) positioning the body at 'optimal' (smallest normal velocity) points in the incident field; (ii) introducing an initial modulation of the incident velocity field near the body; (iii) applying artificial free-surface pressure forcings near free-surface body intersections to suppress large initial surface disturbances; (iv) allowing the body dimension to grow initially from a small value to the actual size; and (v) allowing the body boundary to possess an initial permeability which gradually vanishes.

Based on systematic tests (Xue 1997), we find that an effective scheme is obtained using (v). For a fixed no-flux body, a time-varying body permeability is applied by imposing the body boundary condition

$$\phi_n(\boldsymbol{x},t) = C(t)\left[\frac{\partial}{\partial n}\phi_I(\boldsymbol{x},t) - Q(t)\right], \qquad \boldsymbol{x} \in \mathscr{B}(t), \tag{2.6}$$

where $Q(t)$ is introduced to ensure (global) mass conservation and is given by

$$Q(t) \equiv \frac{\displaystyle\int\!\!\int_{\mathscr{B}(t)} \phi_n(\boldsymbol{x},t)\mathrm{d}S}{\displaystyle\int\!\!\int_{\mathscr{B}(t)} \mathrm{d}S}. \tag{2.7}$$

In (2.6), the time-dependent function C is chosen to vary smoothly from unity (complete permeability) to zero (no-flux) over some time δT:

$$C(t) = \begin{cases} \cos^2\left(\dfrac{\pi}{2\delta T}t\right), & 0 \leqslant t \leqslant \delta T \\ 0, & t \geqslant \delta T. \end{cases} \tag{2.8}$$

In addition to (2.6), it is often also found useful to employ (i) by optimizing the initial placement of the body with respect to the incident field. In our study of the fully nonlinear diffraction of a truncated vertical cylinder (§ 4), for example, we apply (2.8)

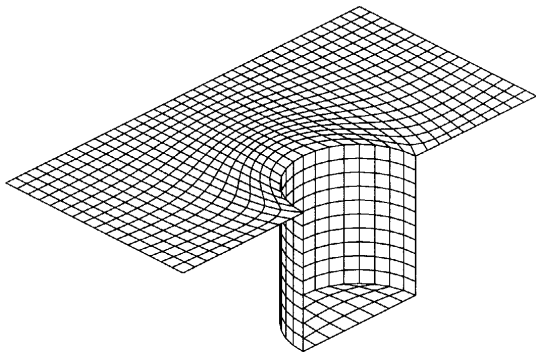

FIGURE 1. Sample QBEM discretization of a surface-piercing vertical truncated circular cylinder. Only half of the symmetric (doubly periodic square) domain is shown.

with δT equal $1/4$ of the incident Stokes wave period, and centre the cylinder initially at a phase of the Stokes wave such that the horizontal velocity of the incident wave at the cylinder surface is minimized at $t \sim \delta T$. As is seen in § 4, this treatment is able to minimize initial transient effects to produce reliable long time predictions.

2.6. *Convergence tests*

We present selected convergence results to illustrate the accuracy and performance of the MEL high-order boundary-element method. Additional convergence tests are given as part of § 3 and § 4, and extensive validation results can be found in Xue (1997).

A key factor in the overall effectiveness of MEL is the efficiency and accuracy of the boundary-value problem solution. We consider a mixed Dirichlet–Neumann boundary-value problem and calculate the maximum error of the QBEM (involving double-node treatment of D–N and N–N intersections) as a function of discretization size. We consider a surface-piercing truncated vertical circular cylinder in a square doubly periodic computational domain. Figure 1 shows a typical discretization using quadratic (iso-parametric) surface elements.

Using a known harmonic solution (with the amplitude of $O(1)$), we impose the Neumann boundary condition on the cylinder and the Dirichlet condition on the free surface and obtain from the solution the maximum errors on the Neumann and Dirichlet surfaces. Figure 2 plots the convergence of these errors as a function the typical grid size Δ. The convergence rate of the maximum error with Δ is shown to be faster than cubic for the potential (Neumann surface) but somewhat less so for its normal derivative (Dirichlet surface). Not indicated in figure 2, but seen in the numerical results, is the fact that the maximum errors generally occur at the Dirichlet–Neumann boundary intersection.

3. Ship bow waves

We investigate in this section the development of three-dimensional ship bow waves using fully nonlinear MEL simulations. Started from rest to constant forward speed in the time-domain simulations, convergent steady-state bow wave profiles are computed for the flared wedge, Wigley, and Series 60 hulls. For the latter two hulls, the present fully nonlinear predictions are validated against available experiments.

An issue of some interest is the importance of three-dimensionality and upstream

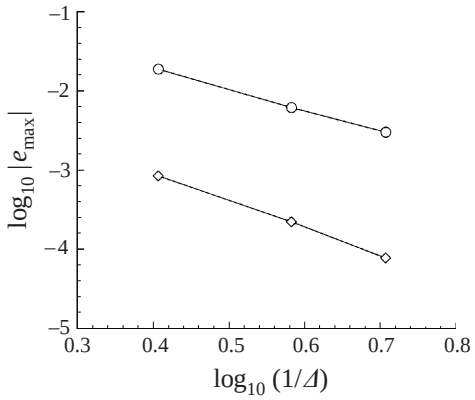

FIGURE 2. Maximum errors ($e_{\max}$) of the QBEM boundary-value problem solution involving mixed Neumann–Dirichlet (N–D) boundary conditions as a function of (typical) grid size Δ. The maximum errors in the potential on the N surface ($\diamond$), and in its normal derivative on the D surface ($\circ$) are plotted separately. The average slopes of these log-log convergence curves are -2.6 and -3.4 for the D and N surfaces respectively.

influence in the development of bow waves. This is evaluated by comparing the present three-dimensional results to those obtained using a nonlinear slender-body quasi-two-dimensional approximation. In the quasi-two-dimensional approach, a slender-body assumption is made to reduce the three-dimensional problem to two-dimensional (parabolic) wave-making problems in a space-fixed reference (y, z)-plane normal to the direction $(-x)$ of the ship motion. A ship bow advancing through this plane is modelled as a two-dimensional wave-maker with its geometry/velocity given by the time-changing bow cross-section in that plane. Use of this quasi-two-dimensional approach has been popular since Chapman (1975) (e.g. Chapman 1976; Yeung & Kim 1981; and recently and specifically for the bow wave problem by e.g. Maruo & Song 1994; Tulin & Wu 1996).

We implement the nonlinear quasi-two-dimensional method in the present work by applying the Cauchy-integral MEL approach of Vinje & Brevig (1981) to solve the two-dimensional wave-making problem. The method is very similar to that in, e.g. Dommermuth *et al.* (1988), and has been validated systematically in terms of convergence with space–time discretizations and conservation of global quantities.

For the fully nonlinear three-dimensional simulation, the ship is located at the centre of a rectangular computational domain, length L and width W, which moves with the ship forward speed. For our simulations, we use typically $L/L_h \sim 2$ and $W/L_h \sim 1$, where L_h is the length of the ship hull. To minimize reflection from the boundary of the computational domain, a region of numerical sponge layer (i.e. damping zone) is placed around the perimeter of the domain. With judicious choices of the width of the damping zone (typically $O(1/6)$ of L and W along the transverse and longitudinal edges), and the damping parameter $\nu(\boldsymbol{x})$ therein (typically a quadratic variation with maximum value at the outer edges), it is shown that effective damping of outgoing waves can be achieved with negligible effect on the steady-state bow wave results. Details can be found in Xue (1997).

Our interest is in the steady-state bow wave, and effects of initial transients are minimized by allowing a varying forward speed $V(t)$ which increases gradually from zero to its steady value U. An acceptable choice is a $\sin^2$ variation of $V(t)/U$ over a period of $O(0.2)L_h/U$. The final results are checked to confirm that they are

independent of changes in the chosen $V(t)$. For the time integration, dynamic time step with Courant number $C_n = 0.2$ and maximum time-step size $\Delta t_{\max} = 0.01 L_h/U$ is used.

3.1. *Flared-wedge bow*

As an initial study, we consider a canonical three-dimensional flared (hyperbolic) wedge-shaped bow geometry which possesses: (i) a simple closed-form geometric specification; (ii) a simple (closed-form) linear slender-body solution (Ogilvie 1972); and (iii) a single parameter quantifying three-dimensionality for given forward speed. The flared-wedge geometry is given by

$$|y| = x(1 + z/D)\tan\alpha, \qquad z/D \geqslant -1, \tag{3.1}$$

where x, y, z are the longitudinal, transverse and vertical coordinates. The flared bow is characterized by a single dimension D which is the (constant) still-water draught. In (3.1), α is half the bow-entry angle at the still-water level ($z = 0$) and is the parameter which measures the three-dimensionality of the bow. Note that (3.1) has a flare given by a longitudinally varying dead-rise angle $\Theta(x) = \arctan[(x/D)\tan\alpha]$.

For (fine) *wall-sided* wedged-shaped bows, an analytic solution is available in the context of linearized slender-body theory (Ogilvie 1972). For flared-wedge bow, the closed-form solution can be generalized. Specifically, we obtain the wave height on the bow to be

$$Z(X) \equiv \frac{\eta(X)}{\alpha F_D D} = \frac{2}{\pi}\int_0^\infty \mu^{-5/2}(\mu - 1 + \mathrm{e}^{-\mu})\sin(\mu^{1/2}X)\mathrm{d}\mu, \tag{3.2}$$

which is a universal curve for $Z(X)$, where $X \equiv x/(F_D D)$, and the Froude number based on D is given by $F_D \equiv U(gD)^{-1/2}$ with g being the gravitational acceleration.

For the (nonlinear) quasi-two-dimensional theory, the quasi-two-dimensional initial boundary-value problem for the velocity potential $\psi(y, z; t \equiv x/U)$, say, can be stated in a straightforward way. For this geometry, the quasi-two-dimensional problem is that of a flap-type wave-maker, hinged at $z = -D$, with normal velocity given by

$$\frac{\partial\psi(y, z, t)}{\partial n} = U\tan\alpha(1 + z/D), \tag{3.3}$$

to be specified on the instantaneous hull position $y = t(1 + z/D)U\tan\alpha$. Since U and α do not appear elsewhere in the quasi-two-dimensional problem (except in the scaling of $x = Ut$), it is interesting to note that, unlike in the actual three-dimensional problem, the forward speed and three-dimensionality parameters do not appear independently but only in the combination $U\tan\alpha$ (or the dimensionless form $F_D\tan\alpha$) in the quasi-two-dimensional formulation. Furthermore, since the quasi-two-dimensional problem does not admit upstream influence ($\psi \equiv 0$ at $t = 0$), the two-dimensional wave-maker problem with impulsive start (3.3) has a singularity at the free surface and wave-maker intersection at initial time $t \equiv x/U = 0+$ (see e.g. King & Needham 1994). Direct numerical solution of this problem, as expected, does not converge with respect to discretization.

Figure 3 plots the quasi-two-dimensional results for the wave profiles on the flared-wedge bow obtained using different spatial discretizations for different values of the parameter $F_D\tan\alpha$. As discussed above, the numerical results do not converge as (average) discretization size $\Delta\ell$ is decreased but becomes increasingly steeper at the bow. In fact they eventually diverge as $\Delta\ell \to 0$. Since downstream values of ψ are obtained as an initial-value problem, the profiles do not converge for any x. Such

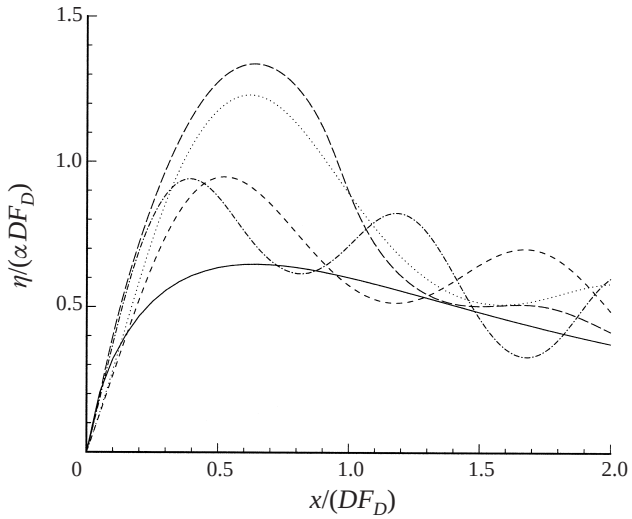

FIGURE 3. Wave profiles on a flared-wedge bow obtained using quasi-two-dimensional simulations with (average) spatial discretization size $\Delta\ell/D$ for $F_D \tan\alpha = 0.08$: $\Delta\ell/D = 0.04$ (- - -), $\Delta\ell/D = 0.025$ (— · —); and $F_D \tan\alpha = 0.16$: $\Delta\ell/D = 0.04$ (· · ·), $\Delta\ell/D = 0.025$ (– – –). For comparison, the linearized slender-body theory result (3.2) (——) is also shown.

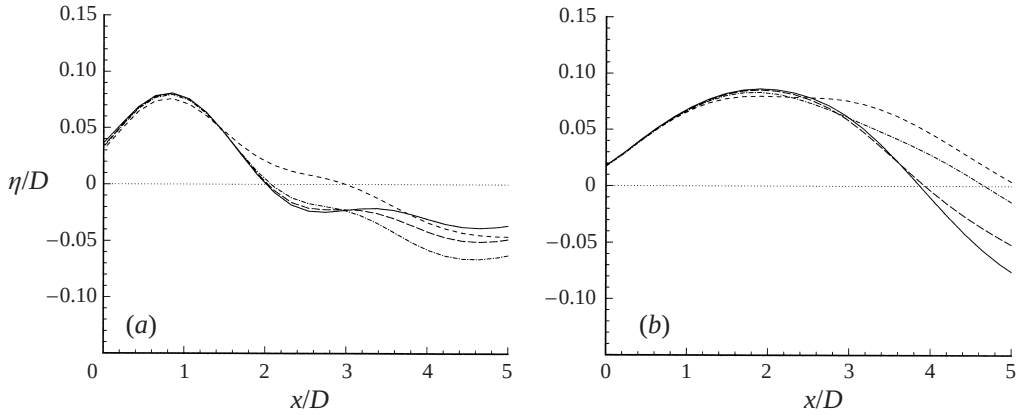

FIGURE 4. Fully-nonlinear three-dimensional MEL simulation results of the evolution of the wave profile on a flared-wedge bow for (*a*) $F_D = 1.0$ and $\tan\alpha = 0.1$ at $Ut/D = 0$ (· · ·), 3.0 (- - -), 4.0 (— · —), 4.5 (– – –), and 5.0 (——); and (*b*) $F_D = 2.0$ and $\tan\alpha = 0.05$ at $Ut/D = 0$ (· · ·), 3.0 (- - -), 4.0 (— · —), 5.0 (– – –), and 6.0 (——).

results can be rendered convergent by introduction of artificial physical or numerical effects into the problem. This is discussed in § 3.2.

For comparison, the linearized slender-body theory result (3.2) is also plotted in figure 3. In normalized coordinates, the theoretical result is independent of $F_D \tan\alpha$. For small X, where the quasi-two-dimensional profiles are close, (3.2) provides a correct asymptotic behaviour, $Z \sim (2X/\pi)(1 - \gamma - 2\log X)$ as $X \to 0$, where $\gamma = 0.577\ldots$ is Euler's constant. For larger X, the linearized and nonlinear (quasi-two-dimensional) slender-body results differ qualitatively even for a small value of $F_D \tan\alpha$. Comparing the linearized and nonlinear profiles, it is clear that nonlinearity plays an important role even for relatively small values of $F_D \tan\alpha$.

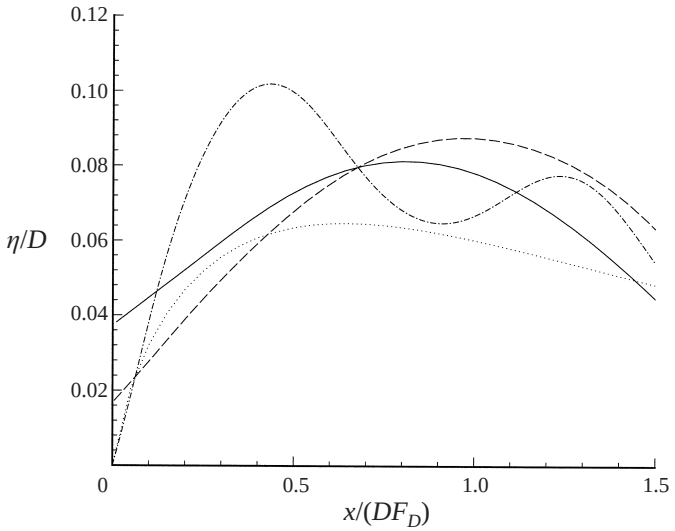

FIGURE 5. Comparison of the steady-state wave profiles on a flared wedge-shaped bow among fully nonlinear three-dimensional computations with $F_D = 1$ and $\tan\alpha = 0.1$ (——) and $F_D = 2$ and $\tan\alpha = 0.05$ (– – –); quasi-two-dimensional results for $F_D \tan\alpha = 0.1$ (— · —), and linearized slender-body theory (· · ·).

Full three-dimensional nonlinear simulations using MEL QBEM are also obtained (for these three-dimensional simulations, we close the body at $L_h/D = 8$ with a streamlined aft body). To isolate the three-dimensional effect, we consider two different cases which have the same parameter value $F_D \tan\alpha = 0.1$ but different F_D and α — Case 1: $F_D = 1$ and $\tan\alpha = 0.10$; and Case 2: $F_D = 2$ and $\tan\alpha = 0.05$. Figure 4 shows the time evolution of the bow wave profiles which monotonically approach steady state. In both cases, steady state is reached up to $x(F_D D)^{-1} \sim O(1)$ after time $Ut/D \sim O(4)$.

Figure 5 compares the bow wave profile predictions for Cases 1 and 2 among steady-state result of fully nonlinear three-dimensional simulation, nonlinear quasi-two-dimensional simulation, and linearized slender-body theory. As pointed out earlier, since $F_D \tan\alpha$ is constant, the quasi-two-dimensional theory predicts the same profile for different F_D (in the normalized X coordinate). For the full three-dimensional problem, different combinations of F_D and $\tan\alpha$, as expected, lead to qualitatively different bow wave profiles as a function of X. Another qualitative difference between three-dimensional and slender-body theories is the finite wave height at the bow stem predicted by the former but absent in the two-dimensional theories. Quantitatively, the nonlinear slender-body calculation tends to over-predict the maximum bow wave height (and hence the initial profile slope) but otherwise obtains a comparable magnitude further downstream. When nonlinearity is ignored, the linearized theory is inadequate and underestimates the overall wave amplitude significantly.

The nonlinear three-dimensional prediction of finite bow stem wave height can be compared to the modified slender-body theory of Fontaine & Faltinsen (1997) which accounts for (linear) upstream effects in the neighbourhood of the bow stem. For $(F_D, \tan\alpha) = (1, 0.1)$ and $(2, 0.05)$, Fontaine & Faltinsen's (1997) theory obtains (for wall-sided wedge bow) bow stem wave heights of $0.032D$ and $0.016D$ respectively. These are to be compared to the fully nonlinear three-dimensional predictions in figure 5 of $0.038D$ and $0.017D$ respectively. As expected, the discrepancy

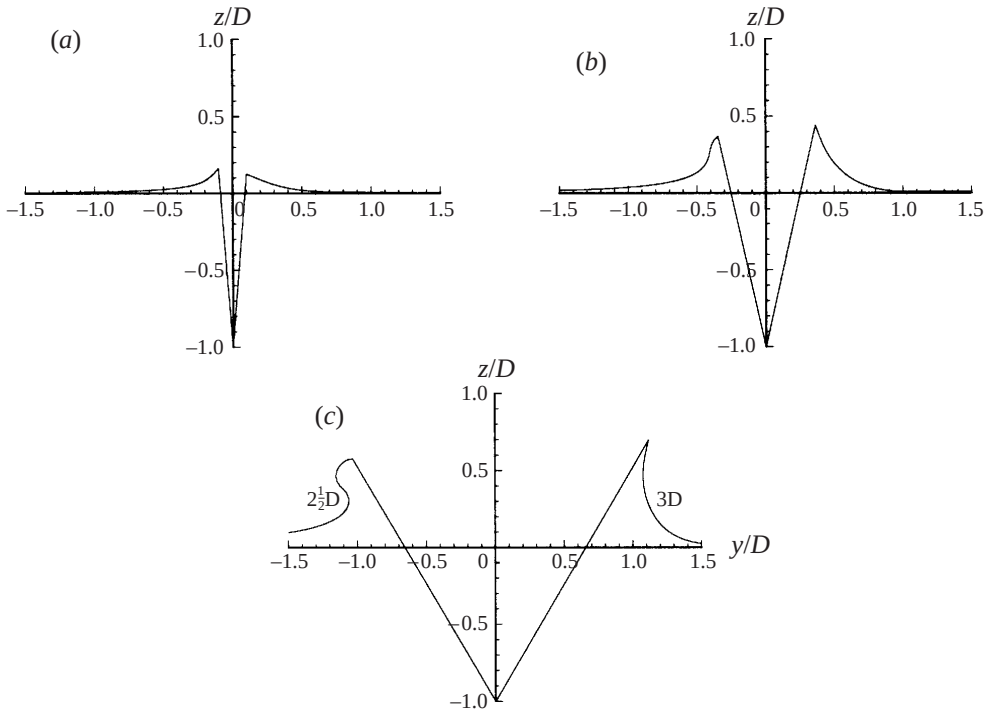

FIGURE 6. Comparison of transverse bow wave profiles, around a flared-wedge hull started smoothly from rest, obtained using: quasi-two-dimensional (left) and three-dimensional (right) nonlinear simulations for $(x/D, Ut/D) = (a)\ (0.36, 1.28)$; $(b)\ (1.02, 2.00)$; and $(c)\ (2.64, 3.62)$. The hull reaches a constant speed of $F_D = 2$ after $Ut/D = 2$.

is smaller for smaller α. These comparisons underscore the importance of accounting for three-dimensional effects even for thin (wedge) bows (at least near the bow stem).

An interesting bow wave development problem that can be considered in the present context is that associated with the transient, say start-up, motion. In this case, the quasi-two-dimensional formulation for this bow does not possess a singularity at the stem and a convergent result can be obtained. We consider, for illustration, the case $\tan\alpha = 0.25$ and $F_D = 2$ which is reached smoothly over a period of $Ut/D = 2$.

Figure 6 compares the fully nonlinear three-dimensional results with the quasi-two-dimensional solutions for the transverse bow wave profiles at selected positions and times. At early time, figure 6(a) for $Ut/D = 1.28$, the quasi-two-dimensional result over-predicts the wave height on the hull (cf. figure 5). At later times (figure 6b), however, the three-dimensional hull wave height exceeds the quasi-two-dimensional prediction. Some time later, in the absence of three-dimensional interactions, the quasi-two-dimensional bow wave soon overturns (figure 6c), while the three-dimensional wave height continues to increase without breaking. (The three-dimensional bow wave eventually reaches much higher up the hull and finally breaks at an aft location where the dead-rise angle $\Theta(x)$ of the flared wedge becomes large.) Thus, transient quasi-two-dimensional computations tend to over-predict (predict earlier) wave breaking and as a result under-predict the maximum bow wave height attained. This appears to be true under rather general conditions (see e.g. Part 1, figure 11).

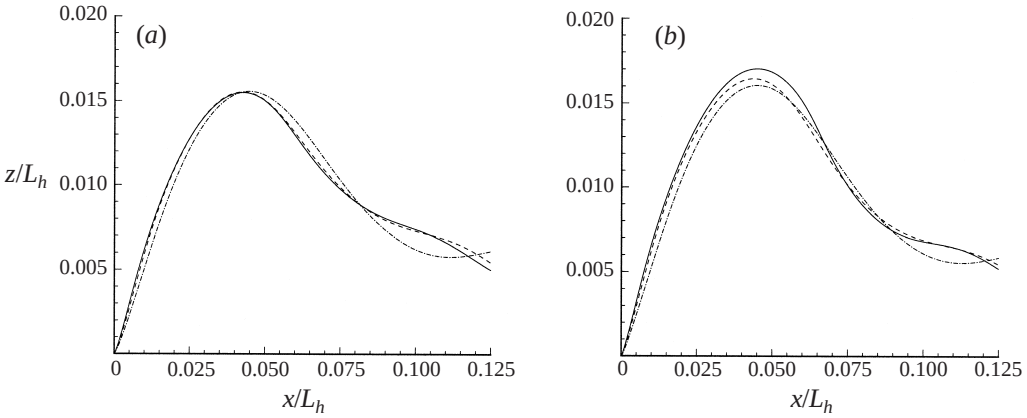

FIGURE 7. Quasi-two-dimensional simulation results of the bow wave profiles on a Wigley hull, $F_r = 0.316$, with bow stem rake angle $\beta =$ (*a*) 5° and (*b*) 2.5°; obtained using (average) discretization size $\Delta\ell/L_h = 0.001$ (— · —); 0.0005 (- - -); and 0.00025 (——).

3.2. *Wigley and Series 60 ship hulls*

We now consider more realistic ship hulls for which experimental measurements of bow waves are available for comparison.

3.2.1. *Wigley hull*

The Wigley hull geometry is specified by

$$\frac{y}{B/2} = \frac{4x}{L_h}(1 - x/L_h)[1 - (z/D)^2], \qquad 0 \leqslant x \leqslant L_h, -D \leqslant z \leqslant 0, \tag{3.4}$$

with length, beam and draught L_h, B and D respectively. For illustration, we consider the case given by $B/L_h = 0.1$ and $D/L_h = 0.0625$.

As in the flared-wedge case, quasi-two-dimensional results for the steady-state bow wave do not converge as a result of the impulsive wave-maker problem singularity at small time. An interesting approach to obtain a convergent result for this case is proposed by Maruo & Song (1994) (see also Tulin & Wu 1996) who introduced a small (typically 5°) artificial rake angle in the (otherwise vertical) bow stem. We implement this treatment to obtain convergent predictions (as a function of finite rake angle) and compare these to three-dimensional results to assess the practical utility of the former and the importance of three-dimensionality for bow waves on such hulls.

Figure 7 shows the convergence of the quasi-two-dimensional results for the bow wave profiles with $\Delta\ell$ for different (fixed) rake angles β. The Froude number is $F_r \equiv U(gL_h)^{-1/2} = 0.316$. For $\beta = 5°$, figure 7(*a*), a convergent value of the maximum wave height is obtained. When β is reduced, figure 7(*b*) for $\beta = 2.5°$, there is no evidence of convergence even for very small $\Delta\ell$. Significantly, as shown in figure 8, the quasi-two-dimensional predictions turn out to be sensitive to the (small) values of β.

We obtain steady-state bow wave profiles for this hull using a three-dimensional MEL simulation. A compilation of computational and experimental results for $F_r = 0.316$ is shown in figure 8. The convergence to steady state of the fully nonlinear three-dimensional results (obtained using $O(300)$ and $O(3000)$ quadratic elements on the hull and free surface respectively) is obtained readily for $x/L_h \sim 0.15$ after $tU/L_h \sim O(0.3)$. These compare favourably with experimental data with less than

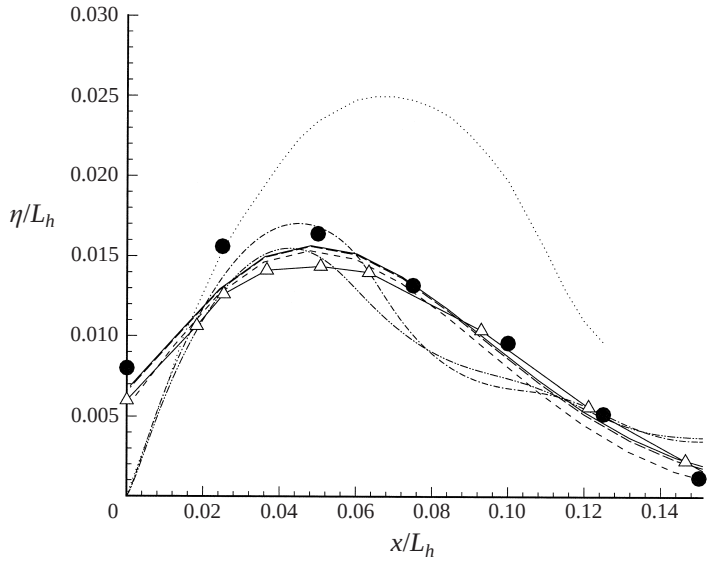

FIGURE 8. Comparison of computed and measured steady-state bow wave profile on a Wigley hull, $F_r = 0.316$. The results shown are: three-dimensional MEL profiles at $tU/L_h = 0.25$ (- - -), 0.30 (– – –), 0.35 (——); steady Dawson method calculation of Raven (1993) (△); quasi-two-dimensional slender-body theory computations obtained with $(\Delta\ell/L_h, \beta) = (0.0005, 0°)$ (· · ·), $(0.00025, 2.5°)$ (— · —), $(0.00025, 5°)$ (— · · —); and experimental measurements of Miyata (1980) (•).

5% discrepancy for the predicted peak wave height. The bow wave amplitude at the stem is also predicted well with differences likely to be attributable to the presence of spray in the physical experiment. The present results also compare well to ship wave computations which assume steady state. As an example, a result of Raven (1993) obtained using a (steady) Dawson method is plotted in figure 8. We remark that compared to the steady-state approaches, the present time-domain scheme is more powerful since it can simulate the complete transient development of the (steady and) unsteady bow waves till breaking (cf. figure 6).

The quasi-two-dimensional results in figure 8 show the lack of convergence as $\beta \to 0$ (the results are convergent with grid size $\Delta\ell$ only for $\beta > 5°$). For the 'typical' value of $\beta = 5°$ (Tulin & Wu 1996), the prediction is acceptable only for larger distance from the stem. The importance of three-dimensional effects is thus evident even for this unusually slender hull ($B/L_h = 0.1$).

3.2.2. *Series 60 hull*

Finally we consider a more realistic hull geometry, a Series 60 ($C_b = 0.6$) hull. For this hull, apparent discrepancies regarding details of the flow near the bow are reported in a recent comparison among experimental data and different computational methods (cf. Ship Research Institute 1994).

In the fully nonlinear three-dimensional MEL simulation, we use $O(200)$ and $O(2000)$ QBEM elements on the hull and free surface, respectively. In the simulation, the hull is shortened to $0.5L_h$ of which the forward $0.2L_h$ replicates exactly the bow of the Series 60 hull in order to reduce computational cost. Through convergence tests, this is shown not to affect the accuracy of the bow wave results. For $F_r = 0.316$, the steady state of the wave in the bow region is reached after $tU/L_h > O(0.5)$. Figure 9 plots the three-dimensional wave field around the hull at $tU/L_h > O(0.5) = 0.6$.

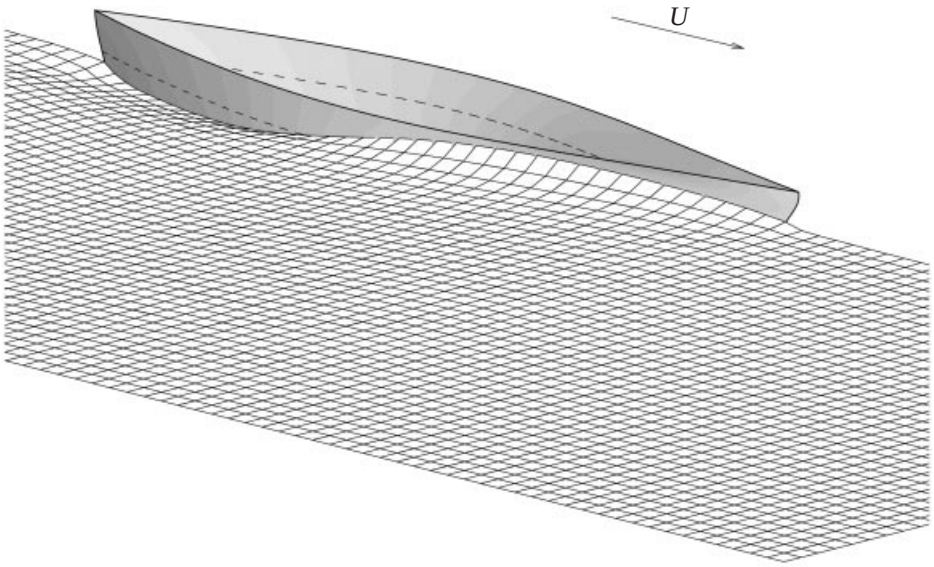

FIGURE 9. The (bow) wave field around a Series 60 ($C_b = 0.6$) hull with $F_r = 0.316$ at $tU/L_h = 0.6$. The wave field is symmetric with respect to the centre-plane of the hull. The dashed line denotes the still water line. The result is obtained using the fully nonlinear three-dimensional MEL simulation.

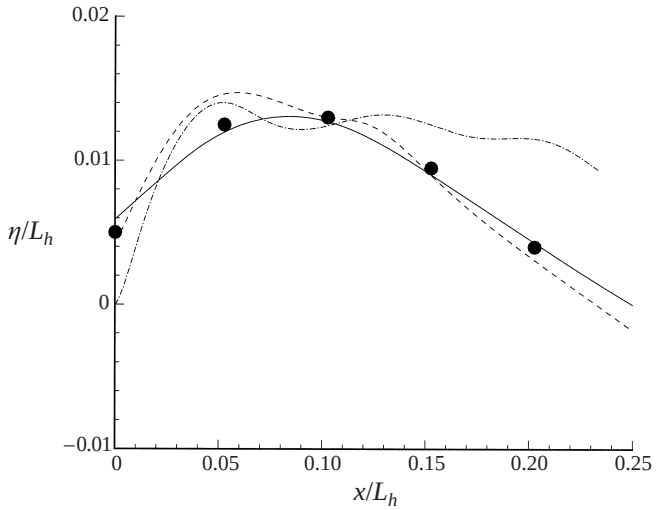

FIGURE 10. Comparison of computed and measured steady-state bow wave profile on a Series 60 ($C_b = 0.6$) hull, $F_r = 0.316$. The results shown are: (converged) three-dimensional MEL profile at $tU/L_h = 0.6$ (——); RANS computations of Tahara & Stern (1994) (- - -); quasi-two-dimensional slender-body theory computations obtained with $\Delta\ell/L_h = 0.005$ (— · —); and experimental measurements of Stern *et al.* (1995) (•).

The steady-state bow wave profile is shown in figure 10. For comparison, the latest measurement data for this case (Stern, Longo & Zhang 1995) are plotted. The overall good comparison is remarkable. The present potential flow formulation does not contain some of the physics present in the experiments, some of which are modelled in Reynolds-averaged Navier–Stokes (RANS) computations. In figure 10, we plot, for comparison, a steady RANS result of Tahara & Stern (1994). The

overall comparison is acceptable. Despite the presence of viscous effects in RANS, it somewhat over-predicts the maximum wave height relative to the experiments and the MEL simulations.

The present Series 60 hull possesses a natural rake angle of $\beta \approx 6^\circ$ which reduces the convergence difficulty of the quasi-two-dimensional simulations. The convergence of quasi-two-dimensional results with grid size $\Delta\ell$ is nevertheless very slow (see Xue 1997 for details). Figure 10 contains a quasi-two-dimensional result (using $\Delta\ell/L_h = 0.0005$, which has more or less converged over the domain shown). As expected, the predictions are not satisfactory near the bow stem. The poor performance further downstream (in comparison to figure 8, for example), however, is notable and may indicate a limit of validity of the slender-body theory with respect to hull geometry.

4. High-harmonic wave excitations on a surface-piercing cylinder

We consider the fully nonlinear three-dimensional wave diffraction by a surface-piercing body in a Stokes incident wave. Our main interest is the quantification of the higher-harmonic wave diffraction forces which may be associated with high-natural-frequency resonant excitations or 'ringing' of large compliant offshore structure (e.g. Davies *et al.* 1994; Krokstad & Stansberg 1995).

To be specific, we perform a fully nonlinear three-dimensional MEL simulation of the diffraction of an exact (two-dimensional) Stokes wave train (Schwartz 1974) by a surface-piercing vertical truncated circular cylinder radius R and (still water) draught D. The Stokes wave has wavelength $\lambda = 2\pi/k$, fundamental period $T = 2\pi/\omega$, and steepness kA. We consider the initial-value problem (cf. §2.5) to obtain the nonlinear (horizontal) force history $F(t)$. The simulations are continued until (limit-cycle) steady state $F(t)$ is obtained from which we obtain the harmonic force amplitudes and phases by Fourier analysis.

The nonlinear force $F(t)$ is computed by direct integration of the pressure on the instantaneous wetted body. The pressure is given by Bernoulli's equation which can be written in a form following the moving grid:

$$p = -\rho\left[\frac{\mathrm{d}\phi}{\mathrm{d}t} + \left(\tfrac{1}{2}\nabla\phi - \boldsymbol{V}_g\right)\cdot\nabla\phi + gz\right], \tag{4.1}$$

where we follow the grid-fixed potential ϕ, with grid velocity given by $\boldsymbol{V}_g$. (An alternative approach which solves the BVP again to directly obtain $\partial\phi/\partial t$ in the Bernoulli equation is also implemented as a check. The results are almost identical. Details are in Xue 1997.)

The approach to steady state of the normalized complex amplitudes of the harmonic components is monitored by using Fourier integration over moving time:

$$f^{(0)}(t) = (kA)^{-2}\frac{1}{T}\int_t^{t+T} F(\tau)\mathrm{d}\tau, \tag{4.2}$$

$$f^{(m)}(t) = (kA)^{-m}\frac{2}{T}\int_t^{t+T} F(\tau)\mathrm{e}^{\mathrm{i}m\omega\tau}\mathrm{d}\tau,\ m = 1, 2, \ldots, \tag{4.3}$$

where the leading-order magnitudes of the harmonics are factored out. The amplitude of $f^{(m)}(t)$ is simply $|f^{(m)}(t)|$, while its phase (relative to the incident wave) is

$$\theta^{(m)}(t) \equiv \frac{1}{m}\left\{\arg[f^{(m)}(t)] + 2n\pi\right\}, \qquad m = 1, 2, \ldots,\ n = 0, \pm1, \pm2, \ldots\ . \tag{4.4}$$

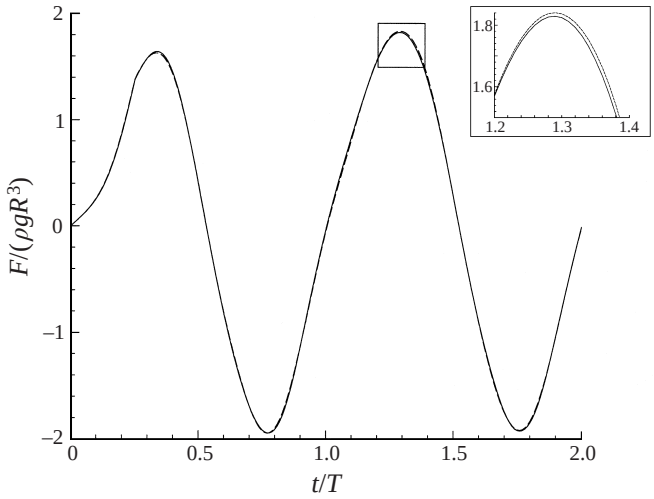

FIGURE 11. Time history of the nonlinear longitudinal force $F(t)$ on a vertical circular cylinder in Stokes incident waves ($kA = 0.3$, $kR = 0.3$, $D/R = 3$). Three-dimensional MEL simulations are obtained using $N_c = 16$ (——) and 24 (- - -) nodes along the circumference of the cylinder.

4.1. *Convergence tests*

To establish convergence of our simulations and ultimately the reliability of the high-harmonic force predictions, extensive numerical tests are performed (see Xue 1997). For illustration, we present selected results for a case with $kA = 0.3$, $kR = 0.3$ and $D/R = 3$. For spatial discretization, we use $N_c \times N_z$ QBEM nodes on the vertical cylinder surface. With $N_z = N_c/2$, and accounting for elements on the cylinder bottom, we have a total of $9N_c^2/64$ (9-node) quadratic elements on the body surface. We use a doubly periodic computational domain of length $L/\lambda = 1$ and width $W/L = 0.6$ (the total number of free-surface quadratic elements is approximately $0.006N_c^2LW/R^2$). For time evolution, we use dynamic time stepping with $C_n = 0.2$ and $\Delta t_{\max} = T/100$. Due to the transverse symmetry of the problem, only half of the computational domain and cylinder are used (see figure 1).

All our simulations are checked for conservation of mass and energy. For two different discretizations $N_c = 16$ and 24, total mass/energy (normalized by their initial values) are conserved to within $O(10^{-6})/O(10^{-3})$ and $O(10^{-7})/O(10^{-4})$ respectively. The conservation of mass, in particular, validates the treatment of the diffraction problem associated with (2.6).

Figure 11 shows the time history $F(t)$ of the longitudinal force on the cylinder obtained using $N_c = 16$ and 24. We note the absence of transients at small time and the apparent approach to a limit cycle in $t/T \sim O(1)$ (simulation time $t_S = O(2T)$, cf. (4.3)).

The convergence of the force harmonic amplitudes (4.3) with (simulation) time is of primary interest. This is shown in figure 12 for the amplitudes and phases for $m = 0, 1, 2, 3, 4$ obtained using two different spatial discretizations N_c. Generally speaking, steady-state values are reached earlier for lower-order harmonics as is convergence with N_c.

4.2. *Numerical predictions of harmonic wave loads*

Our main interest is to predict the (steady-state) harmonic force amplitudes/phases using fully nonlinear time-domain (MEL) simulations. In particular, we seek to

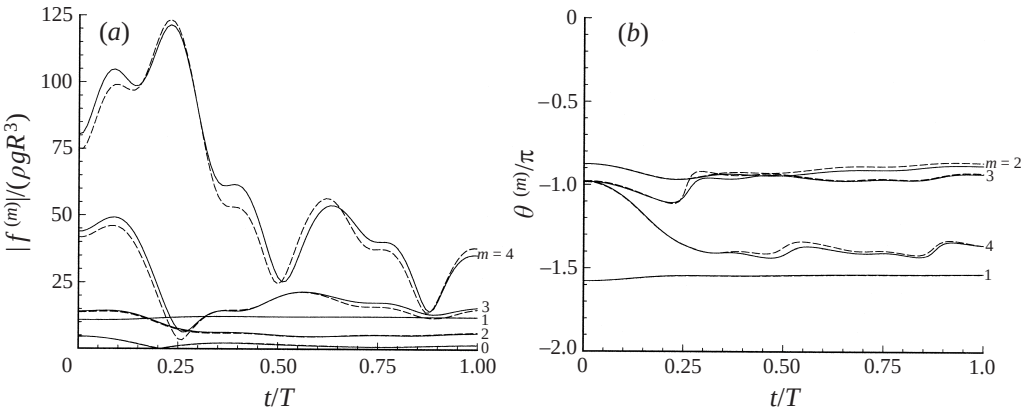

FIGURE 12. Time evolutions of the harmonic components of the nonlinear longitudinal force $F(t)$ on a vertical circular cylinder in Stokes incident waves ($kA = 0.3$, $kR = 0.3$, $D/R = 3$): (*a*) amplitudes $|f^{(m)}|(t)$, and (*b*) phases $\theta^{(m)}(t)$ for harmonics $m = 0, 1, 2, 3, 4$. Three-dimensional MEL simulations are obtained using $N_c = 16$ (——) and 24 (- - -) nodes along the circumference of the cylinder.

obtain predictions up to third harmonic $m = 3$, for which experimental (ringing force) data are available. For the regular (exact) Stokes incident waves, we study three wavelengths (relative to body dimension) given by $kR = 0.22$, 0.29 and 0.39; and three wave amplitudes to wavelength ratios: $kA = 0.130$, 0.148 and 0.20 (A/R varies from 0.34 to 0.91). (These particular choices of parameters are motivated by the high-harmonic force measurements of Krokstad & Stansberg 1995.)

Based on convergence considerations such as those in §4.1 (more extensive convergence results are in Xue 1997), we use $N_c = 24$, and continue simulations up to $t_S = O(5T)$. With this t_S, a (doubly periodic) computational domain size $L = 3\lambda$ and $W = 1.5\lambda$ is found to be sufficient. With these computational parameters, for all cases, we conserve relative mass and energy to within $O(10^{-7})$ and $O(10^{-4})$ respectively; and expect convergence in $f^{(m)}$ to less than $O(1\%)$ for $m = 0, 1$ and 2; and well within $O(5\%)$ for $m = 3$.

The result of a typical fully nonlinear three-dimensional simulation ($kR = 0.39$ and $kA = 0.20$) is shown in figure 13 which plots the instantaneous ($t/T = 1.34$) elevation contours for the total and the diffracted wave fields. At this instant, the up-wave ($\theta = \pi$) run-up reaches its maximum value. Note that the diffracted wave amplitude is large in the near vicinity of the body where the maximum local (total) wave steepness reaches about twice that of the incident wave.

Figure 14(*a*) plots the instantaneous total wave run-up on the cylinder corresponding to figure 13. The fully nonlinear MEL result is compared to that obtained using linearized theory (e.g. Mei 1983). For reference, the (nonlinear) Stokes incident wave run-up is also plotted. For this incident wave steepness ($kA = 0.2$), the maximum nonlinear run-up is $\sim 80\%$ higher than the incident wave. Thus, the nonlinearity of the problem is significantly augmented by the diffraction effect. In contrast, the linearized result underestimates the maximum diffracted wave amplitude by more than a factor of two. At this instant, the diffracted (total minus incident) wave amplitude is much smaller on the downstream side of the cylinder (cf. figure 13). This is found to be generally true throughout the wave period.

The above result for wave diffraction is, of course, dependent on the relative wavelength kR. Figure 14(*b*) plots the fully nonlinear wave run-up on the cylinder

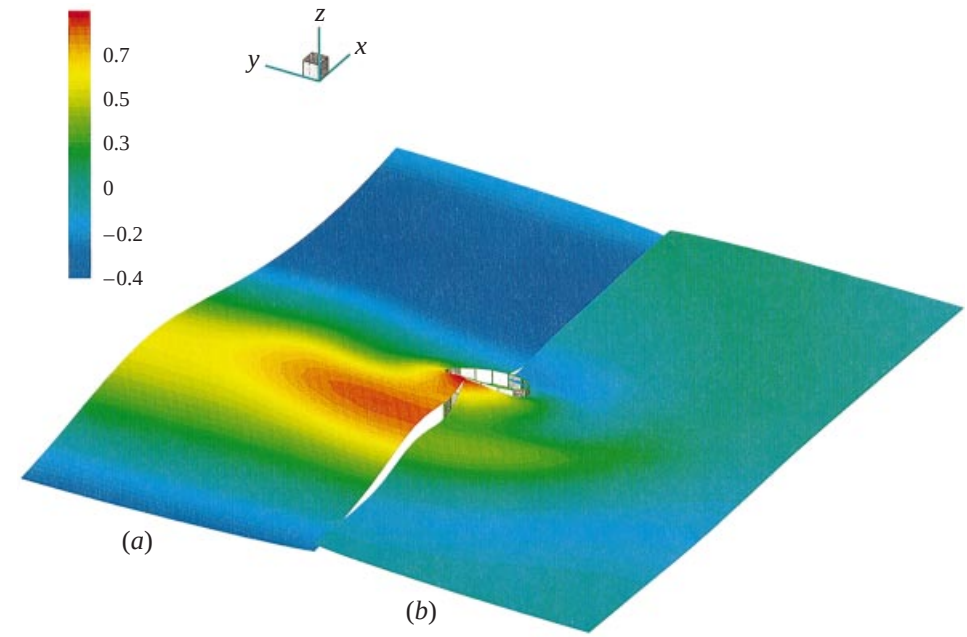

FIGURE 13. Instantaneous (at $t/T = 1.34$) free-surface elevation for (*a*) the total, and (*b*) *twice* (for more colour contrast) the diffracted wave fields for the fully nonlinear interaction of an exact Stokes wave with a truncated vertical circular cylinder ($D/R = 3$, $kR = 0.39$, $kA = 0.20$). The incident wave direction is towards the upper right.

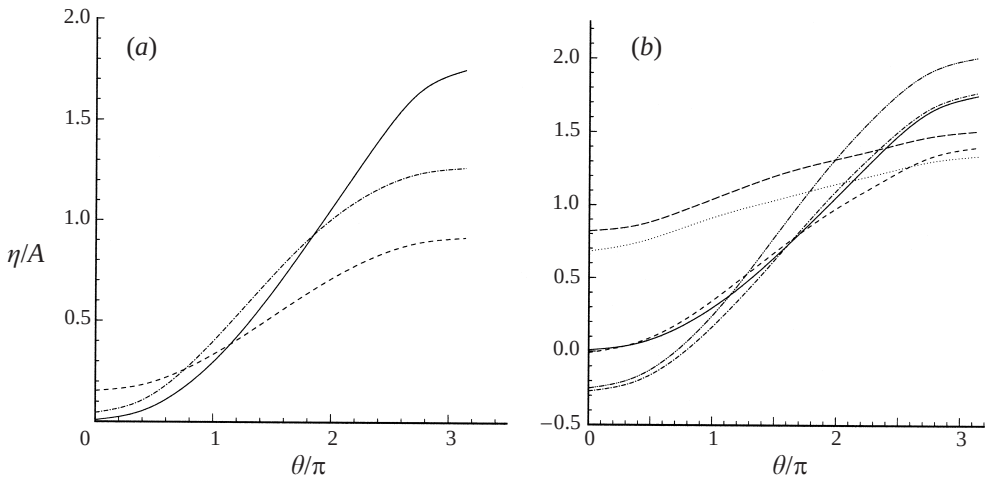

FIGURE 14. Instantaneous wave run-up (corresponding to maximum height on the up-wave point $\theta = \pi$) on a truncated vertical circular cylinder ($D/R = 3$) in Stokes incident waves. (*a*) $kR = 0.39$, $kA = 0.2$ for: fully nonlinear MEL results (——); linearized theory (— · —); and incident Stokes wave (- - -). (*b*) Fully-nonlinear MEL results for $(kR, kA) = (0.29, 0.1)$ (· · ·); $(0.29, 0.2)$ (– – –); $(0.39, 0.1)$ (- - -); $(0.39, 0.2)$ (——); $(0.50, 0.1)$ (— · —); and $(0.60, 0.1)$ (— · · —).

for a range of kR (and different kA). As expected, the diffraction effect increases markedly as kR increases (from small values). Significantly, in this range of kR, the diffracted wave amplitude, and hence nonlinearity, increases more due to increasing kR than kA (compare e.g. the cases $(kR, kA) = (0.29, 0.2)$ versus $(0.6, 0.1)$).

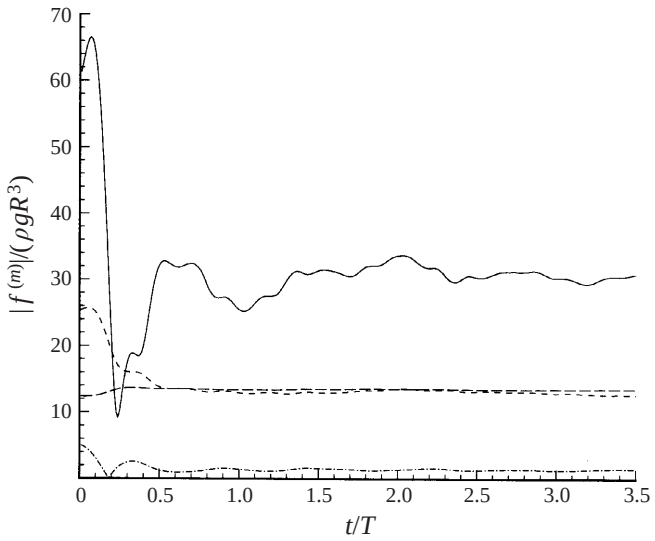

FIGURE 15. Time evolution of the magnitude of the harmonic components, $|f^{(m)}|$, $m = 0$ (— · —), 1 (– – –), 2 (- - -) and 3 (——), of the nonlinear longitudinal force $F(t)$ on a vertical circular cylinder in Stokes incident waves ($kR = 0.22$, $kA = 0.133$, $D/R = 3$).

	$\|f^{(1)}\|/(\rho g R^3)$		$\|f^{(2)}\|/(\rho g R^3)$	
	$kR = 0.22$	$kR = 0.39$	$kR = 0.22$	$kR = 0.39$
MARINTEK	13.64	11.07	10.85	3.04
MEL	13.41	11.18	12.97	2.87
KY	13.28	10.99	14.86	4.38
FNV	13.93	11.31	16.64	9.85

TABLE 2. Comparisons of the first- and second-harmonic force amplitude $|f^{(1)}|$ and $|f^{(2)}|$ on a truncated vertical cylinder ($D/R = 3$) among experimental measurements (Krokstad & Stansberg 1995, MARINTEK), fully nonlinear (MEL) simulations, second-order frequency-domain (axisymmetric) computations (Kim & Yue 1989, KY), and (frequency-domain) small-body asymptotic theory of Faltinsen *et al.* (1995, FNV). For MARINTEK and MEL, $kA = 0.133$ and 0.148 for $kR = 0.22$ and 0.39 respectively.

First- and second-harmonic forces

To provide further validation of our predictions, we obtain first- and second-harmonic force amplitudes and compare these to existing theories and experiments. Figure 15 shows the approach to steady state of the harmonic amplitudes ($m = 0, 1, 2, 3$) for the present problem (with $kR = 0.22$, $kA = 0.133$). At $t/T = O(3.5)$, the (normalized) coefficient $|f^{(1)}|$ has converged to less than 1%, while $|f^{(2)}|$ exhibits a small oscillation of less than 2% amplitude.

Table 2 shows the comparisons of our predicted $|f^{(m)}|$, $m = 1, 2$ (MEL) with experimental measurements (Krokstad & Stansberg 1995, hereafter MARINTEK), second-order frequency-domain (axisymmetric) computations (Kim & Yue 1989, hereafter KY), and the (frequency-domain) small-body asymptotic theory of Faltinsen *et al.* (1995, hereafter FNV).

	$kR = 0.22$	$kR = 0.29$	$kR = 0.39$
MARINTEK	0.27	0.48	0.50
MEL	0.33	0.47	0.50
FNV	0.30	0.51	0.95
MM	0.28	0.52	0.97

TABLE 3. Comparisons of the third-harmonic force amplitude $|f^{(3)}|k^3/(\rho g)$ on a truncated vertical cylinder ($D/R = 3$) among experimental measurements (MARINTEK); fully nonlinear (MEL) simulations; small-body asymptotic theory (FNV); and the third-order (frequency-domain) theory (MM). For MARINTEK and MEL, $kA = 0.133$, 0.130 and 0.148 for $kR = 0.22$, 0.29 and 0.39 respectively.

It should be pointed out that the fully nonlinear time-domain prediction differs from frequency-domain results (even for the first harmonic) because the former, in general, contains all other nonlinear interactions also operating at this harmonic (cf. e.g. Liu, Dommermuth & Yue 1992). In this sense, the frequency-domain result of harmonic m is merely the leading-order term of the fully nonlinear mth harmonic amplitude. With this understanding, the differences between MEL and KY predictions are expected to increase with nonlinearity. Thus the differences between MEL and KY in table 2 increase with kA and kR, as expected.

Comparing MEL to MARINTEK, the values for $|f^{(1)}|$ agree to about $1 \sim 2\%$, while for $|f^{(2)}|$ the discrepancies are in the range $6 \sim 19\%$. In contrast, FNV substantially over-predicts the harmonic amplitudes in all cases, with the over-prediction increasing rapidly with increasing kR. This is not unexpected since FNV is formally a low-kR and low-kA theory with a range of validity for the wavelength likely to be lower than the kR range considered here (see e.g. Malenica & Molin 1995).

Third-harmonic force

This is the case of main interest in the context of ringing excitations. Table 3 compares the values of $|f^{(3)}|$ obtained from: fully nonlinear (MEL) simulations; experiments (MARINTEK); small-body asymptotic theory (FNV); and the third-order (frequency-domain) theory of Malenica & Molin (1995, hereafter MM). We remark here that both FNV and MM are (so far) available strictly only for the uniform vertical circular cylinder geometry.

Considering that the quantities in question are third order (in wave steepness), the present MEL results compare remarkably well with the experimental measurements of MARINTEK with the differences between the two within $O(2\%)$ for the shorter incident wavelengths $kR = 0.29$ and 0.39, and $O(20\%)$ for the longer wavelength $kR = 0.22$. In the physical experiment, the lower $kR \sim 0.22$ case has an associated Keulegan–Carpenter number $K_c \equiv \pi A/R \sim 2$, and non-potential flow effects may play a (minor) role. To assess this, we add a Morison-type quadratic drag term to $F(t)$:

$$F_D(t) = F(t) + \rho R C_D \int_{-D}^{\eta} U|U|\mathrm{d}z, \tag{4.5}$$

where C_D is an empirical drag coefficient, and $U = U(z,t)$ is the (nonlinear) incident wave field velocity on the central axis of the cylinder. With $C_D = 1$, we obtain $|f_D^{(3)}|k^3/(\rho g) = 0.291$ which halves the original difference and is now $\sim 12\%$ above

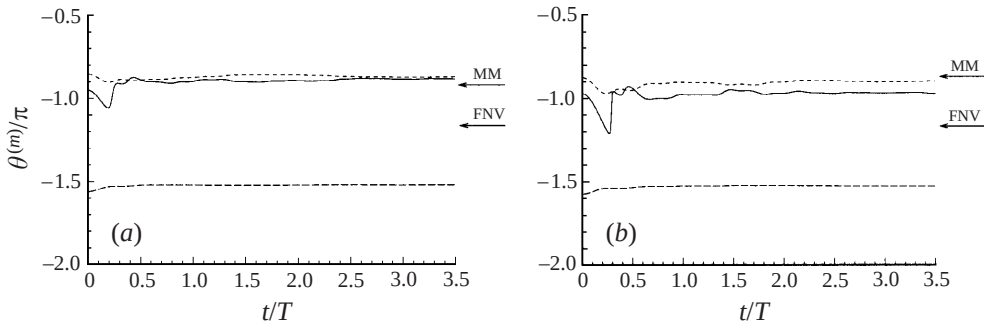

FIGURE 16. Phases (relative to incident wave) of the longitudinal force harmonics on a vertical circular cylinder ($D/R = 3$) in Stokes incident waves: (*a*) $kA = 0.133$, $kR = 0.22$; and (*b*) $kA = 0.130$, $kR = 0.29$. The results shown are: fully nonlinear MEL $\theta^{(m)}(t)$, $m = 1$ (– – –); 2 (- - -); 3 (——); and frequency-domain predictions of $\theta^{(3)}$ from MM and FNV.

the measurement value. For the cases with $KR = 0.29$ and 0.39, $K_c = 1.4$ and 1.2 respectively and non-potential flow effects are much less important.

The frequency-domain perturbation theories compare reasonably well to each other and acceptably so relative to MEL and experiments for the smaller kR cases. As kR increases, FNV and MM increasingly over-predict $|f^{(3)}|$, and, for the $kR = 0.39$ case we studied, they exceed measurements and fully nonlinear computations by almost a factor of 2. As noted earlier, fully nonlinear time-domain MEL differs from frequency-domain perturbation theories because, in addition to the leading-order term(s) perturbation theories predict, MEL contains also higher-order nonlinear contributions at a given harmonic. Such higher-order contributions increase with nonlinearity. From earlier results (cf. figure 14), we note that nonlinearity increases due to two independent factors: increase in the incident wave steepness kA, and increase in the (local) diffracted wave steepness which generally increases with the diffraction parameter kR. Our computations and experimental measurements indicate that, for this range of kR, the latter factor is dominant. This explains the substantially larger discrepancies in the frequency-domain perturbation results for larger kR.

For the range of kR in table 3, the FNV and MM predictions of $|f^{(3)}|$ agree reasonably well with each other. As will be shown in figure 17, appreciable differences in $|f^{(3)}|$ appear for $kR > 0.4$. This deviates somewhat from the results of MM which show a large discrepancy between FNV and MM (in the contribution associated with the product of the first- and second-order potentials) even for very small kR (50% difference for $kR \sim 0.035$).

The significant difference between FNV and MM, however, is the prediction of the phase $\theta^{(3)}$ of $f^{(3)}$. According to FNV, $\theta^{(3)} = \pi/6 + 2n\pi/3$ (for some integer n) and is independent of kR. As expected, $\theta^{(3)}$ from the complete (arbitrary kR) third-order MM varies with kR. Figure 16 shows the time histories of $\theta^{(m)}$, $m = 1, 2, 3$ from fully nonlinear MEL simulations for two values of kR (see Xue 1997 for additional cases). For the simulation time used, the time histories have long approached their limit-cycle values. These values can be compared to the (frequency-domain) predictions of FNV and MM, which are also shown. The present fully nonlinear predictions tend to agree with MM. The comparison is better for lower kR values (as expected from the discussions of the diffracted wave nonlinearity earlier). On the other hand, the FNV predictions differ appreciably for these values of kR.

Systematic MEL computations similar to the above are conducted. Our selection of

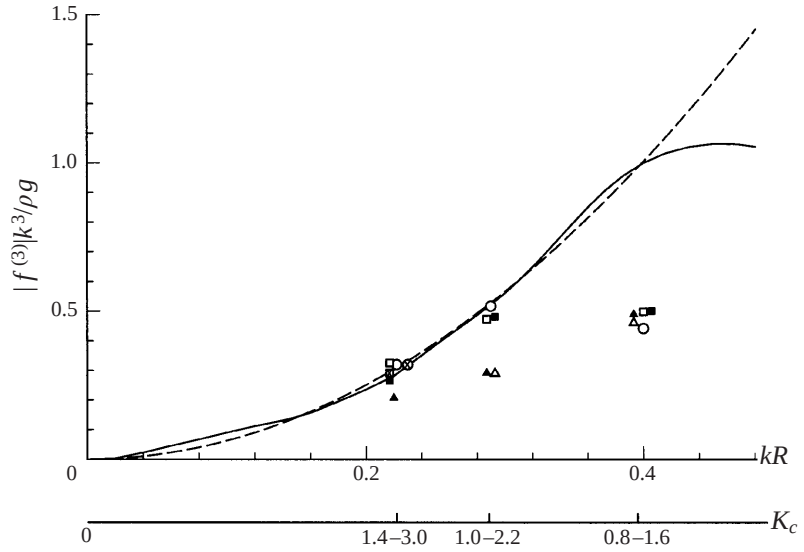

FIGURE 17. Third-harmonic 'ringing' horizontal wave force amplitude $|f^{(3)}|k^3/\rho g$ for a surface-piercing vertical circular cylinder ($D/R = 3$) in Stokes incident waves of different (relative) wavelengths kR and amplitudes kA. The results shown are: experimental measurements, MARINTEK for $kA \sim 0.15$ (■) and 0.20 (▲); and fully nonlinear MEL simulations for $kA \sim 0.10$ (⊗/○, with/without drag correction), 0.15 (■/□, with/without drag correction) and 0.20 (△). The range of Keulegan–Carpenter numbers $K_c \equiv \pi A/R$ for the range of kA considered are indicated. For comparison, frequency-domain perturbation results of FNV (- - -) and MM (——) (which are independent of kA after the normalization in $|f^{(3)}|$) are also plotted.

parameters is guided by the experimental cases reported in MARINTEK. Specifically, we consider $D/R = 3$, $kR = 0.22$, 0.29 and 0.39, and the kA range from $0.10 \sim 0.20$. MARINTEK also contains data for $kA \sim 0.25$ which we do not consider. For this value of kA, wave breaking is observed in the MEL results for all three kR, and the simulations are stopped before steady state can be reached. Wave breaking under the same conditions is also reported in MARINTEK.

Figure 17 summarizes the comparisons for the normalized third-harmonic ('ringing') force amplitude $|f^{(3)}|$. Also plotted are the frequency-domain perturbation results of FNV and MM. As mentioned earlier, for the lower kR, flow separation effects may play a role. To provide an assessment, the Keulegan–Carpenter number $K_c \equiv \pi A/R$ (for the range of kA considered) is noted on a second horizontal axis. For the lowest $kR = 0.22$ case, the MEL result with the (Morison-type) drag correction (cf. (4.5)) is also shown.

Considering the fact that $|f^{(3)}|$ is a third-order quantity, the overall excellent agreement between MEL and MARINTEK is remarkable. For $kR = 0.22$, the addition of a Morison-type correction improves the comparison somewhat but the discrepancies are small in either case. In contrast, the FNV and MM predictions are acceptable only for lower kR and smaller values of kA. For the case of $kR = 0.29$, for example, perturbation results are good for $kA < 0.15$ but differ from fully nonlinear simulations and experiments by $O(70\%)$ for $kA \sim 0.20$. As (local diffracted wave) nonlinearity increases with kR, these discrepancies increase and perturbation theories over-predict $|f^{(3)}|$ by $O(100\%)$, for example, for $kR = 0.39$, even for relatively small incident steepness of $kA \sim 0.1$.

We remark finally that the computational parameters for the present MEL simu-

lations are chosen to provide reliable predictions up to $m = 3$ (cf. §4.1). In theory, even higher-order force harmonics $m = 4, 5, \ldots$, can be of interest. These can, in principle, be obtained similarly by direct fully nonlinear MEL computations with suitable choices of computational parameters.

5. Conclusions

We develop effective fully nonlinear mixed-Lagrangian-Eulerian (MEL) simulations using quadratic boundary elements (QBEM) for general three-dimensional wave–body interactions. A number of techniques are developed to improve the efficacy of this method for wave diffraction and radiation problems for surface-piercing bodies. The method is validated extensively using convergence tests and comparisons to perturbation theories and experiments where available.

We apply the method to the study of two nonlinear three-dimensional wave–body problems. The first problem is the development of waves on the bow of an advancing ship. We use MEL simulations to obtain steady-state bow wave profiles for a flared wedge geometry, a Wigley hull, and a Series 60 bow. We obtain excellent comparisons to experimental measurements (available for the latter two hulls). Comparisons are also made to nonlinear slender-body (quasi-two-dimensional) approximations which show the importance of three-dimensionality and upstream influence not generally accounted for in slender-body theories.

The second problem is the fully nonlinear diffraction of incident Stokes waves by a surface-piercing cylinder. Our main interest is the third-harmonic (ringing) wave excitation on the body for which experimental measurements are reported. The MEL predictions compare remarkably well with experiments and provide unequivocal evidence that fully nonlinear wave diffraction is a sufficient mechanism for the so-called ringing phenomenon.

This research is supported financially by grants from the Office of Naval Research whose sponsorship is gratefully acknowledged.

REFERENCES

Chaplin, J. R., Rainey, R. C. & Yemm, R. W. 1997 Ringing of a vertical cylinder in waves. *J. Fluid Mech.* **350**, 119–147.

Chapman, R. B. 1975 Numerical solution for hydrodynamic forces on a surface-piercing plate oscillating in yaw and sway. *Proc. 1st Intl Conf. on Numerical Ship Hydrodynamics.* Washington DC: National Academy Press.

Chapman, R. B. 1976 Free-surface effects for yawed surface-piercing plates. *J. Ship Res.* **20**, 125–136.

Chau, F. P. & Eatock Taylor, R. 1992 Second-order wave diffraction by a vertical cylinder. *J. Fluid Mech.* **240**, 571–599.

Clément, A. 1996 Coupling of two absorbing boundary conditions for two-dimensional time-domain simulations of free surface gravity waves. *J. Comput. Phys.* **126**, 139–151.

Davies, K. B., Leverette, S. J. & Spillane, M. W. 1994 Ringing response of TLP and GBS platforms. *Proc. BOSS'94 Conference* (ed. C. Chryssostomidis), Cambridge, Massachusetts.

Dommermuth, D. G. & Yue, D. K. P. 1987 Numerical simulations of nonlinear axisymmetric flows with a free surface. *J. Fluid Mech.* **178**, 195–219.

Dommermuth, D. G., Yue, D. K. P., Lin, W. M., Rapp, R. J., Chan, E. S. & Melville, W. K. 1988 Deep-water plunging breakers: a comparison between potential theory and experiments. *J. Fluid Mech.* **189**, 423–442.

Faltinsen, O. M., Newman, J. N. & Vinje, T. 1995 Nonlinear wave loads on a slender vertical cylinder. *J. Fluid Mech.* **289**, 179–198 (referred to herein as FNY).

Ferrant, P. 1996 Simulation of strongly nonlinear wave generation and wave-body interactions

using a three-dimensional MEL model. *Proc. 21st Symp. on Naval Hydrodynamics*, *Trondheim*, *Norway*. Washington DC: National Academy Press.

Fontaine, E. & Faltinsen, O. M. 1997 Steady flow near a wedge shaped bow. *Proc. 12th Intl Workshop on Water Waves and Floating Bodies*, *Carry-le-Rouet*, *France* (ed. B. Molin).

Grosenbaugh, M. A. & Yeung, R. W. 1989 Nonlinear free-surface flow at a two-dimensional bow. *J. Fluid Mech.* **209**, 57–75.

Kim, H. M. & Yue, D. K. P. 1989 The complete second-order diffraction solution for an axisymmetric body. Part I. Monochromatic incident waves. *J. Fluid Mech.* **200**, 235–264 (referred to herein as KY).

King, A. C. & Needham, D. J. 1994 The initial development of a jet caused by fluid, body and free-surface interaction. Part 1. A uniformly accelerating plate. *J. Fluid Mech.* **268**, 89–101.

Krokstad, J. R. & Stansberg, C. T. 1995 Ringing load models verified against experiments. *Proc. Intl Conf. on Offshore Mechanics and Arctic Engineering*, *Copenhagen*, *Denmark* (ed. S. K. Chakrabarti, D. Myrhaug, R. C. Ertekin & H. Maeda) (referred to herein as MARINTEK).

Lewy, H. 1950 Developments at the confluence of analytical boundary conditions. *International Congress of Mathematics*, Vol. 1, Cambridge, Massachusetts.

Lin, W. M., Newman, J. N. & Yue, D. K. P. 1984 Nonlinear forced motions of floating bodies. *Proc. 15th Symp. on Naval Hydrodynamics*, *Hamburg* (ed. O. Krappinger). Washington DC: National Academy Press.

Liu, Y., Dommermuth, D. G. & Yue, D. K. P. 1992 A high-order spectral method for nonlinear wave-body interactions. *J. Fluid Mech.* **245**, 115–136.

Malenica, Š. & Molin, B. 1995 Third-harmonic wave diffraction by a vertical cylinder. *J. Fluid Mech.* **302**, 203. Washington DC: National Academy Press. (referred to herein as MM).

Maruo, H. & Song, W. 1994 Nonlinear analysis of bow wave breaking a deck wetness a high-speed ship by the parabolic approximation. *Proc. 20th Symp. on Naval Hydrodynamics*, *Santa Barbara*, *CA*. Washington DC: National Academy Press.

Mei, C. C. 1983 *The Applied Dynamics of Ocean Surface waves.* Wiley Interscience.

Miyata, H. 1980 Characteristics of nonlinear waves in the near field of ships and their effects on resistance. *Proc. 13th Symp. on Naval Hydrodynamics*, *Tokyo*, *Japan.* Washington DC: National Academy Press.

Nakos, D. E., Kring, D. C. & Sclavounos, P. D. 1993 Rankine panel methods for transient free surface flows. *Proc. 6th Intl Conf. on Numerical Ship Hydrodynamics*, *Iowa City*, *IA*. Washington DC: National Academy Press.

Ogilvie, T. F. 1972 The wave generated by a fine ship bow. *Proc. 9th Symp. on Naval Hydrodynamics*, *Paris*, *France.* Washington DC: National Academy Press.

Rainey, R. C. T. 1995 Slender-body expressions for the wave load on offshore structures. *Proc. R. Soc. Lond.* A **450**, 391–416.

Raven, H. C. 1993 Nonlinear ship wave calculations using the RAPID method. *Proc. 6th Intl Conf. on Numerical Ship Hydrodynamics*, *Iowa City*, *IA*.

Schwartz, L. W. 1974 Computer extension and analytic continuation of Stokes' expansion for gravity waves. *J. Fluid Mech.* **62**, 553–578.

Ship Research Institute (SRI) 1994 *Proc. of CFD Workshop Tokyo — an International Workshop for Improvement of Hull Form Designs.*

Stern, F., Longo, J. & Zhang, Z. J. 1995 Detailed bow-flow data and CFD for a Series 60 $C_b = .6$ ship model for Froude number .316. *Proc. 24th American Towing Tank Conference*, *College Station*, *Texas.*

Tahara, Y. & Stern, F. 1994 A large-domain approach for calculation ship boundary layers and wakes for nonzero Froude numbers. *Proc. CFD Workshop*, *Tokyo.* Vol. I.

Tsai, W. T. & Yue, D. K. P. 1996 Computation of nonlinear free-surface flows. *Ann. Rev. Fluid Mech.* **28**, 249–278.

Tulin, M. P. & Wu, M. 1996 Divergent bow waves. *Proc. 21st Symp. on Naval Hydrodynamics*, *Trondheim*, *Norway*. Washington DC: National Academy Press.

Vinje, T. & Brevig, P. 1981 Nonlinear two-dimensional ship motions. Norwegian Institute of Technology, Report R-112-81.

Xue, M., Xü, H. B., Liu, Y. & Yue, D. K. P. 2001 Computations of fully nonlinear three-dimensional wave–wave and wave–body interactions. Part 1. Three-dimensional steep waves. *J. Fluid Mech.* **438**, 11–39.

Xue, M. 1997 Three-dimensional fully nonlinear simulations of waves and wave body interactions. PhD thesis, Massachusetts Institute of Technology, USA.

Yeung, R. W. & Kim, S. H. 1981 Radiation forces on ships with forward speed. *Proc. 3rd Intl Conf. on Numerical Ship Hydrodynamics, Bassin d'Essaia des Carenes, Paris.* Washington DC: National Academy Press.